Journal of Southeast University (English Edition) Vol. 42, No. 1, pp. 12-25 Mar. 2026 ISSN 1003-7985

Theoretical model and numerical simulation research on minimum overburden thickness of TBM excavation based on surrounding rock arching theory

ZHOU Zhong, SUI Yuchao, YAN Haitao

(School of Civil Engineering, Central South University, Changsha 410075, China)

Abstract: Based on the surrounding rock arching and hingeless arch structure theories, a theoretical formula for the minimum overburden thickness was derived. By substituting different mechanical parameters of multiple tunnels at home and abroad into this formula, minimum self-supporting arch formulas under different surrounding rock classes were obtained. Based on the actual engineering case of a dual-mode shield tunnel, a numerical model for the tunnel boring machine excavation mode was established to verify the theoretical formulas. Next, three surrounding rock classes, four soil layer thickness gradients, and twelve overburden thickness gradients were designed, resulting in 144 models formed by the combination of the three factors. Uniform tests were conducted, and the pressure arch heights under different surrounding rock classes were obtained. The results show that in the theoretical formulas, the tunnel radius has a linear positive correlation with the pressure arch height, while the tunnel depth has a linear positive correlation with the square of the pressure arch height. According to numerical simulation results, the pressure arch height increases with the increase of the overburden thickness and then tends toward a critical value of twice the tunnel diameter. Finally, the results of the numerical model are in good agreement with those calculated using the theoretical formulas, verifying the rationality of the established theoretical formulas.

Key words: minimum overburden thickness; tunnel boring machine (TBM); pressure arch; numerical simulation; self-supporting arch

DOI: 10.3969/j.issn.1003-7985.2026.01.002

In alignment with the strategic objective of enhancing China's transportation infrastructure, significant efforts have been made to construct railroads and highway tunnels on a large scale[1-4]. The tunnel boring machine (TBM) excavation method has been widely employed in hard-rock strata due to its ability to facilitate rapid construction, minimize disruption to surrounding rock, and promote personnel safety and operational efficiency[5]. Within the context of TBM tunneling in hard-rock strata, self-stabilization becomes necessary due to the inherent hysteresis of support, requiring the establishment of a self-supporting arch contingent on a specific overburden thickness for safety assurance. Although considerable research has focused on the minimum overburden thickness for TBM tunneling, a comprehensive, systematic theoretical framework for determining it remains to be established. Thus, there exists a significant practical demand for theoretical advancements in this domain.

Currently, three primary methodologies are utilized to study minimum rock cover thickness: the engineering empirical, numerical simulation, and theoretical formula methods. The engineering empirical method comprises various approaches, including the Norwegian empirical method, the Japanese water-influx method, and the top water coal mining method. For instance, Nilsen[6] developed the Norwegian Undersea Tunnel concept, a technology compilation derived from analyzing the statistics of Norwegian-built tunnels, including seawater depth, bedrock depth, rock cover thickness, and rock seismic wave velocity. Hwang et al.[7] developed the Japanese tunnel water influx formula based on Darcy's law to determine optimal rock cover thickness. In China, top water coal mining was proposed for the construction of undersea tunnels[8]. This method determines rock-over thickness by analogizing the safety coal rock columns employed for mining with rock cover thickness in undersea tunnels. Furthermore, the application of engineering empirical methods is characterized by convenience, facile calculations, and widespread application. However, significant discrepancies exist among the rock cover thicknesses of different empirical methods, highlighting the criticality of on-site, experienced personnel.

The widespread adoption of numerical simulation in investigating overburden thickness is driven by its inherent advantages, such as reduced modeling costs and improved result visibility, coupled with the advancement of field engineering techniques. Sun et al.[9] derived a for-

Received 2025-05-19, **Revised** 2025-10-26.

Biography: ZHOU Zhong (1978—), male, doctor, professor, dazhong78@csu.edu.cn.

Foundation items: The National Natural Science Foundation of China (No. 52478426), the Natural Science Foundation of Hunan Province (No. 2024JJ5428).

Citation: ZHOU Zhong, SUI Yuchao, YAN Haitao. Theoretical model and numerical simulation research on minimum overburden thickness of TBM excavation based on surrounding rock arching theory[J]. Journal of Southeast University (English Edition), 2026, 42(1): 12-25. DOI: 10.3969/j.issn.1003-7985.2026.01.002.

mula for the ultimate support pressure of the tunnel working face under various excavation inclinations and seepage conditions, which was subsequently validated through numerical simulation and the formulation of a design procedure for determining optimal overburden thickness. Li et al. [10] applied fracture damage and numerical analysis software to assess displacement changes at a specific point above the tunnel vault (tunnel crown) across different depths, establishing a displacement convergence method for determining the minimum overburden thickness based on convergence data. Sun et al. [11] investigated the soil arch effect employing a two-dimensional (2D) particle flow procedure, uncovering the relationship between the burial depth and the destabilization and damage mechanisms of the soil mass in front of the excavation, including the resulting soil arch zones. Pang et al. [12] developed a mechanical model for overburden damage based on the half-plane theory of elastodynamics. By numerically simulating the damage process using fast Lagrangian analysis of continua in three dimensions (FLAC3D), they highlighted the sensitivities of various control factors to the damage occurring in the overlying rocks. Dong et al. [13] formulated a mechanical model for rock beams in the main roof slab by analyzing overburden movement and deformation mechanisms, determining rock beam fracture ultimate span and deflection. They validated these results through numerical simulation. Liu et al. [14] employed FLAC3D to investigate surface settlement by varying the overburden size and slump zone mechanical parameters. Their results revealed that the overburden thickness significantly influences surface settlement. Peng et al. [15] established a numerical model for underwater tunnel fluid-solid coupling by analyzing the arching behavior of surrounding rock pressure arches along the vertical direction and proposing a determination method for the appropriate underwater tunnel thickness based on the critical plate thickness of the arch. Numerical simulation methods are frequently integrated with empirical engineering approaches for practical applications. Compared with singular empirical methods, the computational results derived from such combined approaches yield more reliable outcomes; however, the construction of such a model requires accurate parameter values and extensive debugging time.

Compared with numerical simulations, the theoretical framework for determining the minimum overburden thickness is still significantly underdeveloped. Most theoretical investigations focused on the overburden column height during mining, barely considering the minimum overburden thickness associated with hard rock TBM excavation. By determining the criteria for overburden sliding damage in mining, Wang et al. [16] formulated a critical coal pillar width for maintaining the stability of the overlying coal seam. Ma et al. [17] employed the Winkler foundation beam model to derive the relationship between rebound modulus, excavation height, ground settlement, internal forces, and stresses under varying cover layers. Yang et al. [18] employed a beam-hinged cantilever beam model to propose a correlation between rock column thickness and mining height. Pan et al. [19] conducted physical modeling tests and numerical simulations to explore the extent of pressure arches in unlined tunnels under different loads. Overall, theoretical formulations offer greater accuracy compared with numerical simulations and engineering empirical methods. However, these formulations lack the numerical solutions provided by simulations, and numerous foundational assumptions diverge from engineering realities.

To address the deficiency of theoretical formulas for selecting the overburden thickness for TBM hard-rock tunneling, numerical simulations typically rely solely on surrounding rock displacement convergence or plastic strain range, lacking a proper mechanistic foundation for determining this thickness. Thus, in this study, the stable state of the surrounding rock during TBM tunneling was analyzed based on the theory of arch formation in surrounding rock, deriving a formula for calculating the minimum overburden thickness. To validate this formula, it was compared with numerical simulation results obtained from the double-mode shield tunnel between Xixiang and Bao'an Stations on the Guangzhou- Dongguan-Shenzhen Intercity Railway. The findings suggested that the theoretical formula performed reasonably and could serve as a reference for practical engineering applications.

1 Calculation of Minimum Overburden Thickness Considering Surrounding Rock Arching Theory

Natural rock masses (especially Class Ⅲ to Class Ⅴ surrounding rocks) typically exhibit significant discontinuity, heterogeneity, and anisotropy. However, under conditions of sufficient confining pressure and limited deformation, their overall mechanical responses can be approximated to those of continuous media. Therefore, the surrounding rock above the tunnel is idealized as an equivalent continuous elastic arch structure, providing a simplified mechanical representation of the load-transfer process in jointed and fractured rock masses. Notably, while not implying that the rock mass is actually continuous or homogeneous, this simplification characterizes the complex discontinuous system comprising joints and fissures through an equivalent continuum with averaged mechanical parameters. Since the TBM operates in an unsupported state during boring, the overlying rock mass must be kept stable. Drawing on the theory of peripheral rock arch formation, the self-supporting structure of the surrounding rock that ensures tunnel stability during TBM excavation can be analyzed as a hingeless arch.

Fig. 1 illustrates a schematic of the loads acting on the tunnel. These were categorized into two: self-weight and water loads, for separate calculations. As shown in Fig. 1, q and p are the vertical and water loads acting on the self-supporting arch, respectively; R is the tunnel radius, and the hingeless arch is circular.

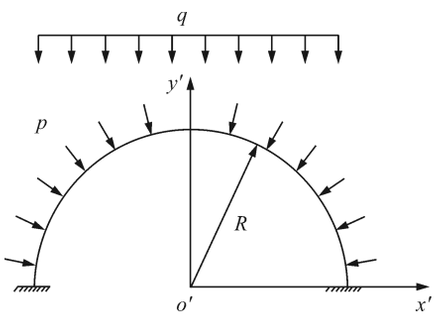

Fig. 1 Tunnel self-supporting arch model

1.1 Operating condition with only deadweight loads

The self-supporting arch under vertical loads is subjected to internal force analysis, yielding the fundamental system of the self-supporting arch based solely on vertical forces (Fig. 2).

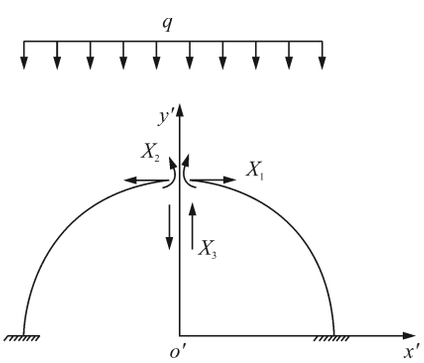

Fig. 2 Basic system of tunnel self-supporting arch considering vertical loads

Fig. 2 shows that the basic arch structure is symmetric and subjected to two symmetric unknown forces (X_1, X_2) and one antisymmetric one (X_3). Therefore, the following expression is derived based on the force law equation:

$$\begin{cases} \delta_{11}X_1 + \delta_{12}X_2 + \Delta_{1q} = 0 \\ \delta_{21}X_1 + \delta_{22}X_2 + \Delta_{2q} = 0 \\ \delta_{33}X_3 + \Delta_{3q} = 0 \end{cases} \tag{1}$$

where the coefficients, δ_{12} and δ_{21}, are rendered zero by the elastic center method; Δ_{iq} represents the displacement generated in the structure along the constraint direction corresponding to the i-th basic unknown quantity (X_i) under load q. The hingeless arches depicted in Figs. 2 and 3 are equivalent, where A_0 represents the half-arch center at 90°. Further, the hingeless arch in Fig. 3 is obtained by segmenting that in Fig. 2 at its apex. This process involves positioning two stiffeners at the ends of the symmetry axis of the cut, with their bases interconnected by stiffeners exhibiting infinite stiffness.

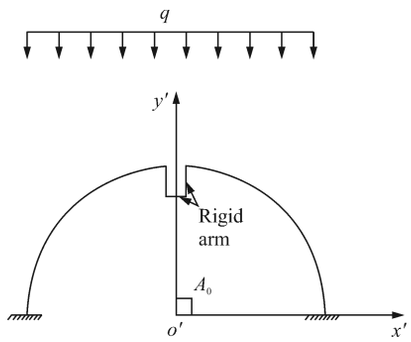

Fig. 3 Tunnel self-supporting arch model diagram considering rigid arm

Fig. 4 shows that the bottom of the rigid arm is cut at point o, introducing the unknown forces, X_1, X_2, and X_3. The force equilibrium equation, described in Eq. (1), is maintained.

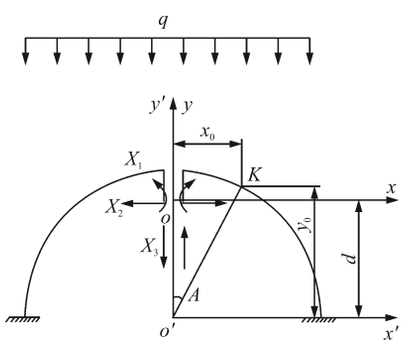

Fig. 4 Basic tunnel self-supporting arch system under vertical load

Further, the flexibility coefficients are obtained by integrating the strain energy expressions associated with unit redundant forces. For a hingeless arch, they are given by

$$\delta_{ij} = \int \left(\frac{\overline{M}_i \overline{M}_j}{EI} + \frac{\overline{F}_{Ni} \overline{F}_{Nj}}{EA} + \frac{k\overline{F}_{Qi} \overline{F}_{Qj}}{GA} \right) \mathrm{d}s \tag{2}$$

where the coefficients $\overline{M}_i$ are the bending moment of the section generated by the i-th unit force; $\overline{F}_{Ni}$ is the corresponding axial force in a specific structural member; $\overline{F}_{Qi}$ corresponds to the shear force in that member under the same unit load; E is the elastic modulus of the material; G is the shear modulus of the material; A is the cross-sectional area; I is the cross-sectional moment of inertia.

For a hingeless symmetric arch, the boundary conditions are as follows: $A = 0, M(0) = 0$; $A = A_0, M(A_0) = M_0$.

When X_1 and X_2 are unit forces, the basic system internal forces are respectively

$$\begin{cases} \overline{M}_1 = 1 \\ \overline{F}_{N1} = 0 \\ \overline{F}_{Q1} = 0 \end{cases} \tag{3}$$

$$\begin{cases} \overline{M}_2 = -y \\ \overline{F}_{N2} = -\cos\varphi \\ \overline{F}_{Q2} = -\sin\varphi \end{cases} \tag{4}$$

where φ is the angle between the member axis and the reference direction.

Thus, δ_{12} is calculated as follows:

$$\delta_{12}=\int\frac{\overline{M}_1\overline{M}_2}{EI}\mathrm{d}s+\int\frac{\overline{F}_{N1}\overline{F}_{N2}}{EA}\mathrm{d}s+\int\frac{k\overline{F}_{Q1}\overline{F}_{Q2}}{GA}\mathrm{d}s \quad (5)$$

Additionally, the substitution of Eqs. (3) and (4) into Eq. (5) yields

$$\delta_{12}=\int-\frac{y}{EI}\mathrm{d}s \quad (6)$$

The new coordinate axes, $x'y'$, are established (Fig. 4), with the x-axis and x' separated by distance d, whereas the y-axis aligns with y'. The relationship between the old and new coordinates in the vertical direction for any point K on the arch axis is represented by the following:

$$y_0=y+d \quad (7)$$

Furthermore, substituting Eq. (7) into Eq. (6) yields the following when δ_{12} is 0:

$$d=\frac{\int\frac{y_0}{EI}\mathrm{d}s}{\int\frac{1}{EI}\mathrm{d}s} \quad (8)$$

The value of the K coordinate system is related to the radius of the arch and the angle of the circle center.

$$\begin{cases}x_0=x=R\sin A\\ y_0=y+d=R\cos A\end{cases} \quad (9)$$

Here, the substitution of Eq. (9) into Eq. (8) obtains d between the centers of elasticity, O, and circle, O', as follows:

$$d=\frac{\int\frac{y_0}{EI}\mathrm{d}s}{\int\frac{1}{EI}\mathrm{d}s}=\frac{2\int_0^{\frac{\pi}{2}}R^2\cos A\,\mathrm{d}A}{2\int_0^{\frac{\pi}{2}}R\,\mathrm{d}A}=\frac{R\sin\frac{\pi}{2}}{\frac{\pi}{2}}=\frac{2R}{\pi} \quad (10)$$

Based on Eq. (10), the bending moment distribution and the corresponding axial force of the arch under a uniform load, q, can be expressed as follows:

$$\begin{cases}M(A)=\frac{qR^2}{2}(1-\cos A)+M_0\\ N(A)=H\cos A+\frac{qR}{2}(1-\cos A)\end{cases} \quad (11)$$

where H is the tunnel depth.

Given the symmetry of the structure, X_3 is zero, implying that δ_{33} is also zero. In this analysis, only the bending moment effect is considered in the displacement calculation. The fundamental bending moment equation under $X_1=1$ and $X_2=1$ actions is given as follows:

$$\begin{cases}\overline{M}_1=1\\ \overline{M}_2=-y=d-y_0=R\left(\frac{\sin A_0}{A_0}-\cos A\right)\end{cases} \quad (12)$$

Therefore, the principal coefficients, δ_{11} and δ_{22}, are

$$\delta_{11}=\int\frac{\overline{M}_1^2}{EI}\mathrm{d}s=2\int_0^{\frac{\pi}{2}}\frac{1}{EI}R\mathrm{d}A=\frac{R\pi}{EI} \quad (13)$$

$$\delta_{22}=\frac{\int\overline{M}_2^2\mathrm{d}s}{EI}=\frac{2\int_0^{\frac{\pi}{2}}R^2\left(\frac{\sin A_0}{A_0}-\cos A\right)^2}{EI}R\mathrm{d}A=\frac{2R^3}{EI}\left(\frac{\pi}{4}-\frac{2}{\pi}\right) \quad (14)$$

The basic equations of mechanics are transformed from Eq. (1) to

$$\begin{cases}\delta_{11}X_1+\Delta_{1q}=0\\ \delta_{22}X_2+\Delta_{2q}=0\end{cases} \quad (15)$$

Next, the free terms, Δ_{1q} and Δ_{2q}, under the basic equation for load bending moment (M_q) are solved as follows:

$$M_q=-\frac{q}{2}x^2=-\frac{q}{2}R^2\sin^2A \quad (16)$$

$$\Delta_{1q}=\int\frac{\overline{M}_1M_q}{EI}\mathrm{d}s=\frac{\int_0^{2\pi}\left(-\frac{qR^2}{2}\sin^2A\right)R\mathrm{d}A}{EI}=-\frac{\pi qR^3}{4EI} \quad (17)$$

$$\Delta_{2q}=\int\frac{\overline{M}_2M_q}{EI}\mathrm{d}s=-\frac{qR^4}{6EI} \quad (18)$$

Furthermore, substituting Eqs. (17) and (18) into Eq. (15) yields the unknown forces X_1 and X_2.

$$X_1=-\frac{\Delta_{1q}}{\delta_{11}}=\frac{-\frac{\pi qR^3}{4EI}}{\frac{R\pi}{EI}}=\frac{qR^2}{4} \quad (19)$$

$$X_2=-\frac{\Delta_{2q}}{\delta_{22}}=\frac{-\frac{qR^4}{6EI}}{\frac{2R^3}{EI}\left(\frac{\pi}{4}-\frac{2}{\pi}\right)}=\frac{\pi qR}{3\pi^2-24} \quad (20)$$

From the above derivation, we obtain the crown bending moment and the springing bending moment as following:

$$M_1=X_1-X_2(R-d)=0.046qR^2 \quad (21)$$

$$M_2=M_q-X_1-X_2d=0.14qR^2 \quad (22)$$

1.2 Operating condition with only water loads

The internal force analysis of the self-supporting arch solely under a water load is depicted in Fig. 5. The basic self-supporting arch system is transformed into a basic structure using the method for solving the internal force of a superstatic structure (Fig. 6).

At this point, the force state of the triangular arch is characterized as follows:

$$\begin{cases}M_q=0\\ F_{Nq}=-pR\\ F_{Qq}=0\end{cases} \quad (23)$$

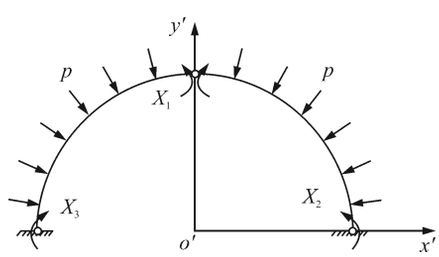

Fig. 5 Basic tunnel self-supporting arch system considering only water load

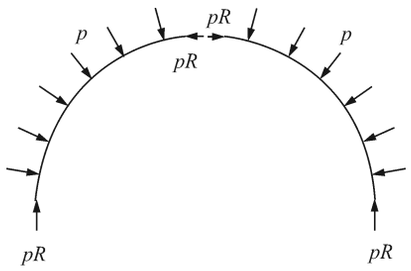

Fig. 6 Equilibrium state of basic structure under water load

Without considering the axial deformation condition, it can be known that the free terms of the force law equation are all zero, i. e. ,

$$\begin{cases} \Delta_{1q} = 0 \\ \Delta_{2q} = 0 \\ \Delta_{3q} = 0 \end{cases} \tag{24}$$

According to the force law equation, it can be determined that X_1, X_2, and X_3 are zero, indicating that the hingeless arch experiences no bending moment under uniform water pressure, thus resulting in the following moment state at the arch foot:

$$M_3 = 0 \tag{25}$$

Therefore, the final bending moment of the arch foot is given by the following if the vertical and water loads of the self-supporting arch are considered:

$$M = M_2 + M_3 = 0.14qR^2 \tag{26}$$

1.3 Calculation formula for thickness of self-supporting arches

The maximum internal tensile stress of the arch is restricted to less than the allowable tensile strength of the rock mass, providing a conservative estimate for preventing tensile cracking and subsequent potential internal failure. Rock masses primarily undergo shear failure or compressive yielding failure under compressive stress; however, the tensile stress condition is still adopted as a simplified stability indicator. Further, as the initiation of tensile stress cracks often precedes large-scale shear failure, it can be considered a sign of instability onset. Moreover, the equivalent mechanical parameters employed in theoretical analysis inherently reflect the comprehensive effect of cohesion and internal friction angle in the Mohr-Coulomb strength envelope.

The maximum cross-sectional tensile stress generated in a hingeless arch structure can be expressed as follows:

$$\sigma_{\max} = \frac{M}{W_Z} \tag{27}$$

$$[\sigma] = \frac{\sigma_t}{n_0} \tag{28}$$

where $[\sigma]$ is the allowable positive bending stress; σ_t is the tensile strength of the rock; n_0 is the safety factor, which is generally estimated as 2-3. 5, and in this paper, it is taken as 3. 5. Incorporating Eq. (25) and W_Z into Eq. (27) yields the following:

$$\frac{0.14\gamma R^2}{h_0^2} \leqslant \frac{\sigma_t}{6n_0} \tag{29}$$

where h_0 is the self-supporting arch thickness; γ is the overlying rock gravity.

For the vertical load q, we obtained the following:

$$q = \gamma(H - h_0) \tag{30}$$

The substitution of Eq. (30) into Eq. (29) yields the following:

$$h_0^2 + \frac{0.84\eta m R^2}{\sigma_t} h_0 - \frac{0.84\eta m R^2 H}{\sigma_t} \geqslant 0 \tag{31}$$

Further, solving Eq. (31) yields the following expression for the thickness of the self-supporting arch:

$$h_0 \geqslant -\frac{0.42\gamma n_0 R^2}{\sigma_t} + \frac{\sqrt{\left(\frac{0.84\gamma n_0 R^2}{\sigma_t}\right)^2 + 3.8\frac{\gamma n_0 R^2 H}{\sigma_t}}}{2} \tag{32}$$

2 Project Cases

Railroad tunnel boring traverses various geological formations characterized by diverse surrounding rock classes. With reference to *Highway Tunnel Design Code*, the mechanical parameters for obtaining tensile strength values of Classes Ⅱ-Ⅴ rocks are presented in Table 1.

Table 1 Parameter selection for different surrounding rock classes

Rock class	W/(kN·m^{-3})	E/GPa	υ	f/(°)	c/MPa	σ/MPa
Ⅱ	27	6.7	0.25	50	1.50	5.0
Ⅲ	25	2.0	0.30	39	0.70	2.0
Ⅳ	23	0.4	0.35	27	0.20	0.3
Ⅴ	20	0.3	0.45	20	0.05	0.2

Note: W is the weight; E is the elastic modulus; υ is Poisson's ratio; f is the internal friction angle; c is the cohesion; σ is the tensile strength.

In this study, 28 local and international tunnels[20] are examined by substituting the mechanical characteristics of various tunnels into Eq. (30). The results of the comparison of the thickness of the self-supporting arches with their respective overburden thickness across various peripheral rock classes are presented in Table 2.

Most of these tunnel projects were executed via TBM excavation, whereas only a few were executed via the drilling-blasting method or NATM under comparable hard-rock geological conditions. These non-TBM tunnel cases are included to cover a broader range of geological variability, allowing for the validation of the proposed formula across a representative spectrum of rock mass strengths and overburden thickness. Thus, the analysis results of these non-TBM hard-rock tunnels remain mechanically comparable. Future studies must expand the

Table 2 Thickness of self-supporting arch across several surrounding rocks of diverse local and international tunnels m

Tunnel name	R	H	h_0				h_{crl}
			Ⅱ	Ⅲ	Ⅳ	Ⅴ	
Vardø	4.1	79.8	7.42	11.02	20.71	27.24	28
Eillingsøy	4.7	130.6	10.94	16.28	30.81	40.82	42
Valderøy	4.7	135.6	11.16	16.61	31.46	41.73	34
Kvalsund	3.7	48.6	5.19	7.67	14.28	18.58	23
Godøy	4.1	144.8	10.12	15.13	28.89	38.71	33
Hvaler	3.8	113.4	8.29	12.38	23.59	31.52	35
Flekkerøy	3.8	93.4	7.49	11.17	21.18	28.14	29
Nappstraumen	4.2	51.6	6.03	8.89	16.44	21.22	27
Fannefjørd	4.1	101.8	8.43	12.55	23.76	31.51	28
Maursund	3.7	84.6	6.94	10.33	19.57	25.97	20
Byfjørd	4.7	223.6	14.46	21.64	41.48	55.80	34
Mastrafjord	4.7	122.6	10.58	15.74	29.73	39.31	40
Freifjørd	4.7	122.6	10.58	15.74	29.73	39.31	30
Hitra	4.7	254.6	15.46	23.17	44.52	60.08	38
Tromsoysund	4.4	92.2	8.56	12.71	23.90	31.44	45
Bjorøy	4.1	76.8	7.27	10.79	20.27	26.62	35
Sloverfjord	4.2	91.6	8.16	12.13	22.87	30.17	40
North Cape	4.0	204.0	11.80	17.69	34.07	46.07	49
Oslofjørd	5.0	124.0	11.29	16.78	31.58	41.60	32
Frøya	4.0	156.0	10.27	15.37	29.44	39.56	41
Ibestad	3.8	117.4	8.44	12.61	24.04	32.16	30
Bomlafjord	4.9	250.2	15.96	23.89	45.81	61.66	35
Skatestraumen	4.0	72.0	6.87	10.19	19.12	25.11	40
Kanmon	5.0	30.0	5.29	7.66	13.57	16.71	11
Kanmon	5.5	38.0	6.56	9.51	16.90	20.87	21
Shin Kanmom	5.4	39.2	6.57	9.53	16.99	21.07	20
Channel tunnel	4.3	106.5	9.03	13.44	25.41	33.64	40

Note: h_{crl} is the arch thickness of the overlying strata.

validation dataset by supplementing more TBM-specific monitoring data to enhance data consistency.

A substitution of the parameters in Table 1 into Eq. (32) yields the formulas for the minimum self-supporting arch thickness across different surrounding rock classes. Additionally, the relationship between the radius, burial depth, and self-supporting arch thickness for various local and international tunnels is depicted in Fig. 7.

The minimum self-supporting arch thickness for Class Ⅱ perimeter rock is

$$h_{min2} = \frac{\sqrt{0.002R^4 + 0.181HR^2 - 0.045R^2}}{2} \quad (33)$$

The minimum self-supporting arch thickness for Class Ⅲ perimeter rock is

$$h_{min3} = \frac{\sqrt{0.011R^4 + 0.420HR^2 - 0.105R^2}}{2} \quad (34)$$

The minimum self-supporting arch thickness for Class Ⅳ perimeter rock is

$$h_{min4} = \frac{\sqrt{0.149R^4 + 1.680HR^2 - 0.386R^2}}{2} \quad (35)$$

The minimum self-supporting arch thickness for Class Ⅴ perimeter rock is

$$h_{min5} = \frac{\sqrt{0.706R^4 + 3.360HR^2 - 0.840R^2}}{2} \quad (36)$$

As shown in Fig. 7, for Classes Ⅱ and Ⅲ perimeter rock, the thickness of the self-supporting arch is positively correlated with both the radius of the tunnel and the thickness of the overburden. Specifically, an increase in either the radius of the tunnel or the overburden thickness results in a greater thickness of the self-supporting arch. In the cases of Classes Ⅳ and Ⅴ perimeter rock, a larger radius and depth of the tunnel similarly correlate with increased thickness of the self-supporting arch.

Given a specific tunnel radius and depth, a higher surrounding rock class corresponds to a greater thickness of the self-supporting arch.

The thickness of the self-supporting arch crown derived from the theoretical formula is slightly smaller than the actual overburden thickness in foreign tunnel projects. The reason is that most domestic and international tunnels are designed using engineering empirical methods, which are relatively conservative. In code methods, the larger the tunnel radius, the greater the depth dividing shallow and deep burial of the tunnel, and the larger the required safety thickness of the self-supporting arch.

This formula allows for the theoretical determination of the thickness of the self-supporting arch for any burial depth and tunnel radius across all perimeter rock classes, thereby providing a reference for establishing reasonable rock cover thickness.

3 Validation of Numerical Simulation Method

3.1 Pressure arch

The pressure arch, formed by the surrounding rock after tunnel excavation, exhibits self-stabilizing characteristics. The trajectory extending from the tunnel arch apex to the ground surface is designated as Path *a*. Some researchers considered the outer boundary of the pressure arch the locus of maximum principal stress deflection, specifically where the horizontal stress equals the vertical stress along Path *a*[21-23]. However, Lü et al. [22] contend that this interpretation is overly conservative, as it neglects the substantial unloading region above the point of maximum principal stress transformation. They argue that, given that radial stresses primarily convert into tangential stresses post-formation of the pressure arch, the point at which the maximum vertical stress begins to diminish may be considered the outer boundary of the pres-

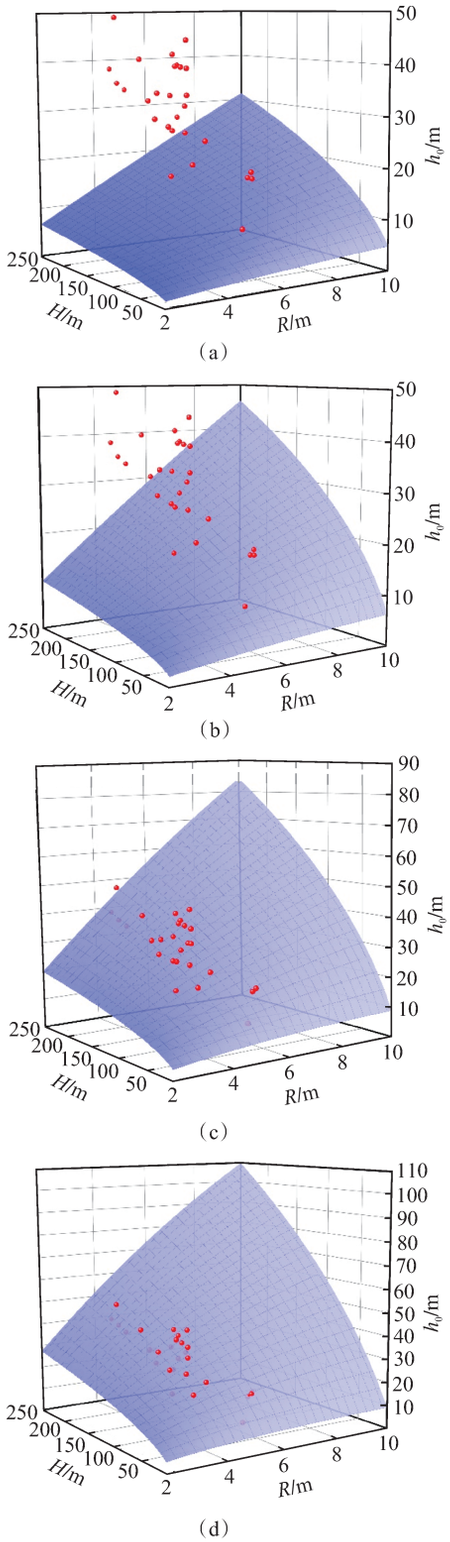

Fig. 7 Comparison of the arch height under different surrounding rock classes and actual tunnel overburden thickness. (a) Class Ⅱ; (b) Class Ⅲ; (c) Class Ⅳ; (d) Class Ⅴ

sure arch. The inner boundary typically appears near the tunnel body.

For the purpose of calculating the height of the pressure arch, this chapter designates the inner boundary at the vault of Path *a*. The height of the pressure arch, denoted as *h*, represents the difference in height between the outer and inner boundaries of the pressure arch, as illustrated in Fig. 8. This section investigates the variations in vertical stress along Path *a* to elucidate the factors influencing the height of the pressure arch.

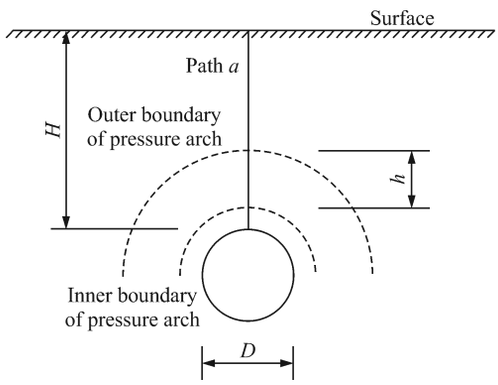

Fig. 8 Schematic of pressure arch height

For Path *a*, the vertical stress gradient is defined as $k = \Delta\sigma_v/\Delta z$, where σ_v and z denote the vertical stress and distance from the tunnel crown, respectively. Concurrently, the quantitative identification criterion for the outer boundary of the pressure arch is the first point that satisfies the following condition: the vertical stress gradient, k, transitions from a positive value to a negative one. Specifically, this transition corresponds to a change in the vertical stress profile: it shifts from increasing with depth (consistent with the original rock stress field) to decreasing with depth (reflecting the shielding effect of the pressure arch).

3.2 Model overview

The double-mode shield tunnel boring along the Guangzhou-Dongguan-Shenzhen Intercity Railway (between Xixiang and Bao'an Stations) serves as a pertinent example. This interval predominantly traverses strata of slightly and moderately weathered granite when utilizing the TBM mode. However, it transitions to the earth pressure balance mode when crossing areas characterized by strongly weathered strata. This mode switching can extend up to half a month (Fig. 9). To expedite the construction timeline, the project proposes a downward adjustment of the original design route to increase the TBM-mode boring distance, thereby reducing the mode change frequency and enhancing boring speed. Key considerations in this process include maintaining the self-stabilization of the surrounding rock and minimizing tunnel depth to decrease tunneling costs, which are central to the study of minimum overburden thickness.

A 2D model of TBM-mode excavation is constructed with the following boundary conditions: lateral constraints are applied to the sides (to restrict horizontal movement), bottom constraints are applied to limit hori-

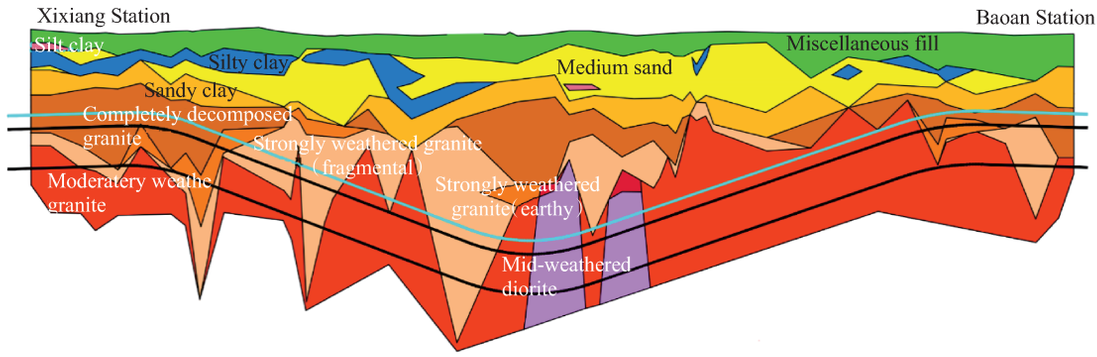

Fig. 9 Schematic of location map of the Xibao Interval

zontal and vertical movements, and no constraints are applied to the top. The soil and hard rock within the model adhere to the Moore-Cullen yield criterion. Additionally, the model dimensions are $80(H_{sf} + h_{crl} + 5D)$, where D is the tunnel diamete and assumed to be 10 m in this numerical simulation; H_{sf} is the pressure arch thickness of soft soil. Fig. 10 shows the schematic of the model. Although pressure arch formation is essentially a three-dimensional (3D) phenomenon involving lateral confinement and transverse load transfer, this study adopts a 2D plane-strain model to represent the central section of a long TBM tunnel. This assumption is widely applied in tunnel mechanics when the tunnel length significantly exceeds its diameter, and when the boundary effects at the portal are negligible.

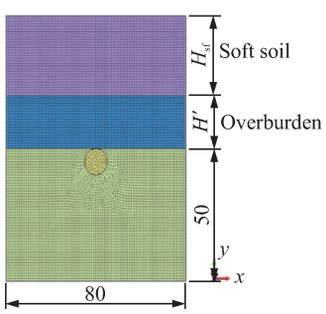

Fig. 10 Schematic of the overall model (unit: m)

In this study, medium and weakly weathered rock layers are classified as hard rock, whereas the remaining rock layers are considered soft soils. Although the shield machine operates in hard rock during TBM-mode excavation, the rock does not exhibit uniform lithology. The actual project predominantly traverses strata classified as Class Ⅲ peripheral rock.

In this study, 144 models are constructed for uniform testing by incorporating 3 enclosing rock classes, 4 soil thickness gradients, and 12 overburden thickness gradients. The resulting pressure arch heights under varying hard rock lithologies were recorded. Tables 3 and 4 detail the geotechnical parameter selection and values of each factor.

The initial stress state is established by evaluating gravitational loads and horizontal in situ stress characterized by the earth pressure coefficient K_0. The vertical and horizontal stresses are defined as $\sigma_v = \gamma H'$ and $\sigma_h = K_0\sigma_v$, respectively, where γ is the unit weight of the rock mass; H' is the overburden thickness; $K_0 = 1 - \sin\varphi'$ is the static earth pressure coefficient (determined by the equivalent internal friction angle of the rock mass φ'). In the numerical simulation, this stress field is applied before tunnel excavation, followed by static stress equilibrium initialization calculations to ensure numerical stability. For shallow-buried tunnels, where in situ stress data cannot be readily measured directly, the proposed method provides a reasonable characterization of their stress conditions. Based on the Xixiang Station-Bao'an Station Section of Work Area 1, Contract Section Ⅱ, Airport-Qianhai Segment of the Sui-Guan-Shen Intercity Railway, the parameters are mainly derived from regional geological survey reports and extant research results on similar lithologies in adjacent TBM tunnel projects.

The surrounding rock stress curves across different overburden thicknesses (0-2.4D) for full-face Class Ⅱ to Class Ⅳ hard rocks are shown in Figs. 11-13, respectively.

Table 3 Parameter selection of rock class and soil mass

Stratum condition	Rock class	W/(kN·m^{-3})	E/GPa	υ	f/(°)	c/MPa
Hard rock layer	Ⅱ	27	6.7	0.25	50	1.50
	Ⅲ	25	2.0	0.30	39	0.70
	Ⅳ	23	0.4	0.35	27	0.20
Soft soil layer	Ⅴ	20	0.3	0.45	20	0.05

Table 4 Value of each factor

Level	Rock class	H_{sf}/m	h_{crl}/m
1	Ⅱ	0	0.4D
2	Ⅲ	D	0.8D
3	Ⅳ	2D	1.2D
4		3D	1.6D
5			2.0D
6			2.4D

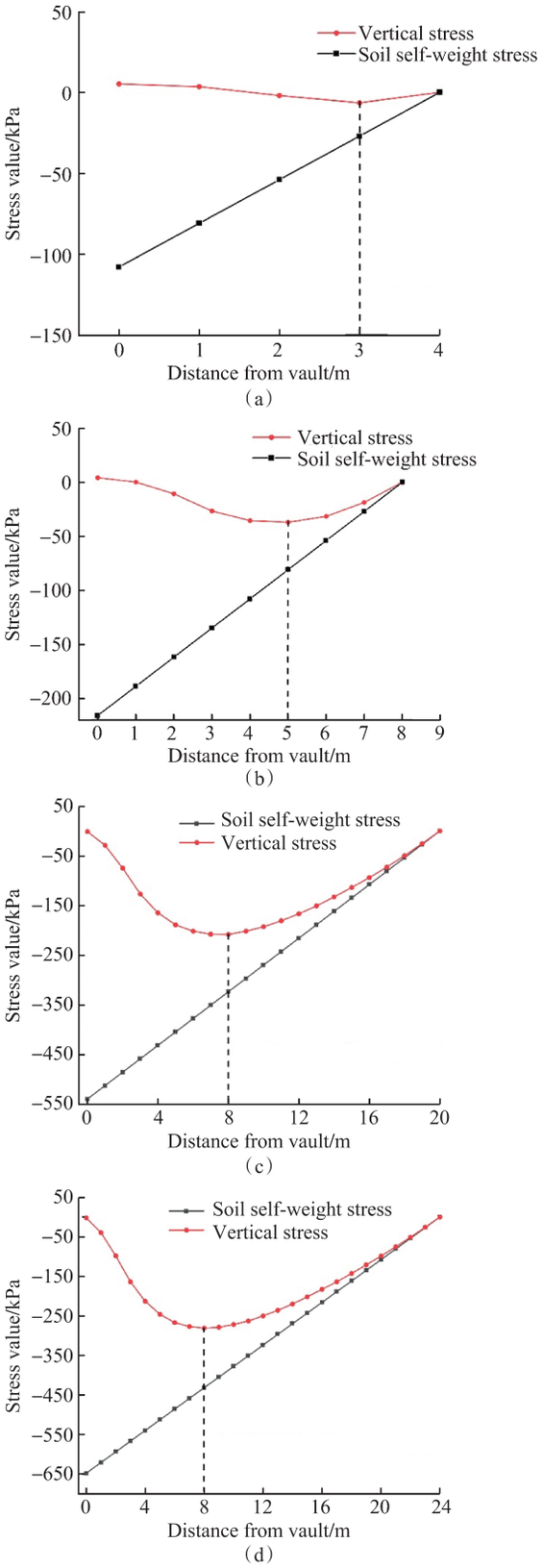

Fig. 11 Stress curves of Class Ⅱ hard rock across various overburden thicknesses. (a) 0.4D; (b) 0.8D; (c) 2.0D; (d) 2.4D

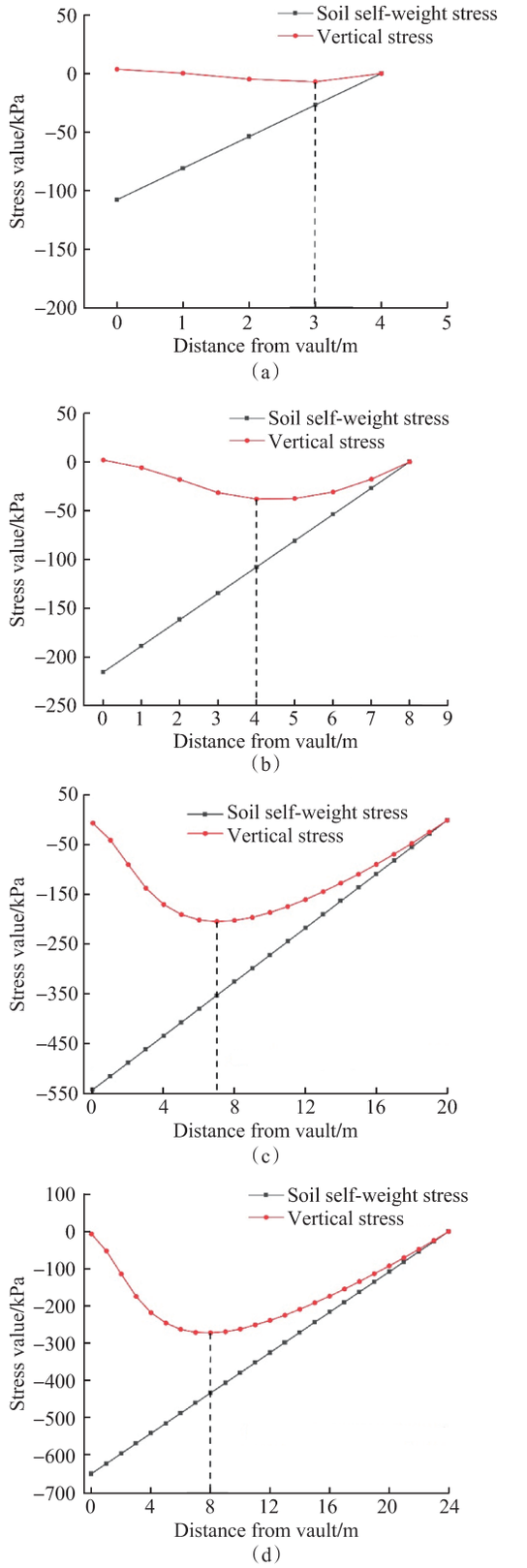

Fig. 12 Stress curves of Class Ⅲ hard rock across various overburden thicknesses. (a) 0.4D; (b) 0.8D; (c) 2.0D; (d) 2.4D

3.3 Analysis of results

Fig. 14 shows the comparison between the numerical simulation and theoretical formulation of the pressure arch height, where eight sections of the Xibao Interval are examined by both approaches. The results are presented in Table 5.

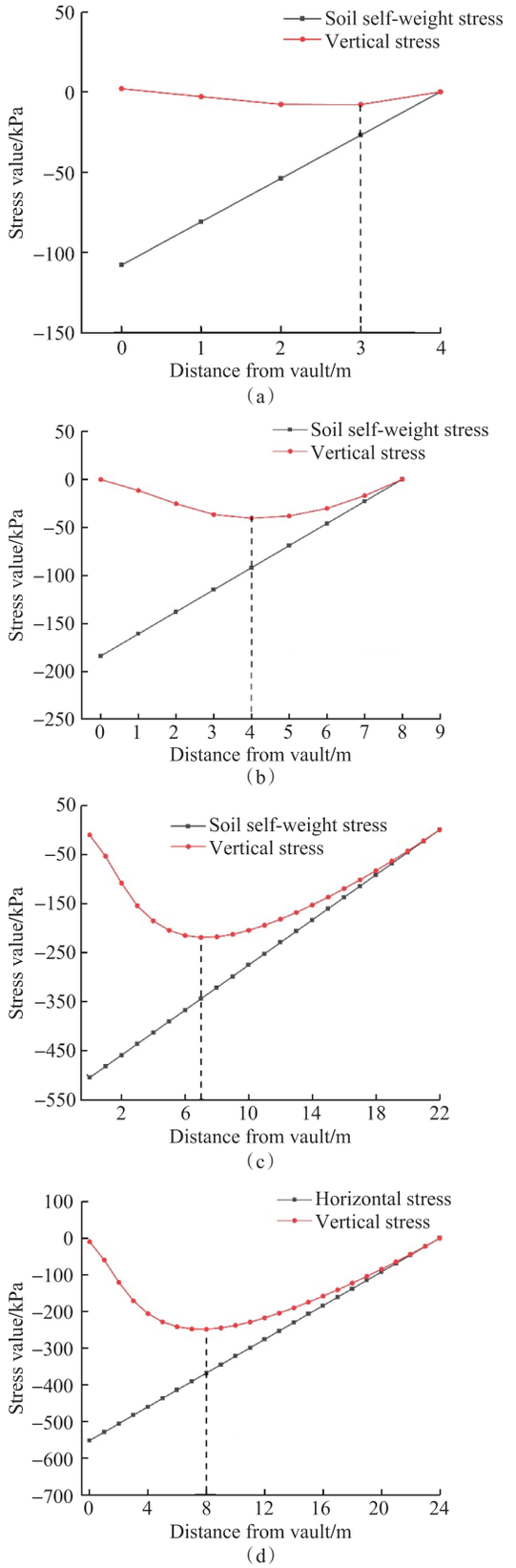

Fig. 13 Stress curves of Class Ⅳ hard rock across different overburden thicknesses. (a) 0.4*D*; (b) 0.8*D*; (c) 2.0*D*; (d) 2.4*D*

The ratio of the height of the outer boundary of the pressure arch to the burial depth was calculated using both numerical simulation and theoretical equation methods across varying overburden thicknesses beneath different soft soil cover layers(Fig. 15).

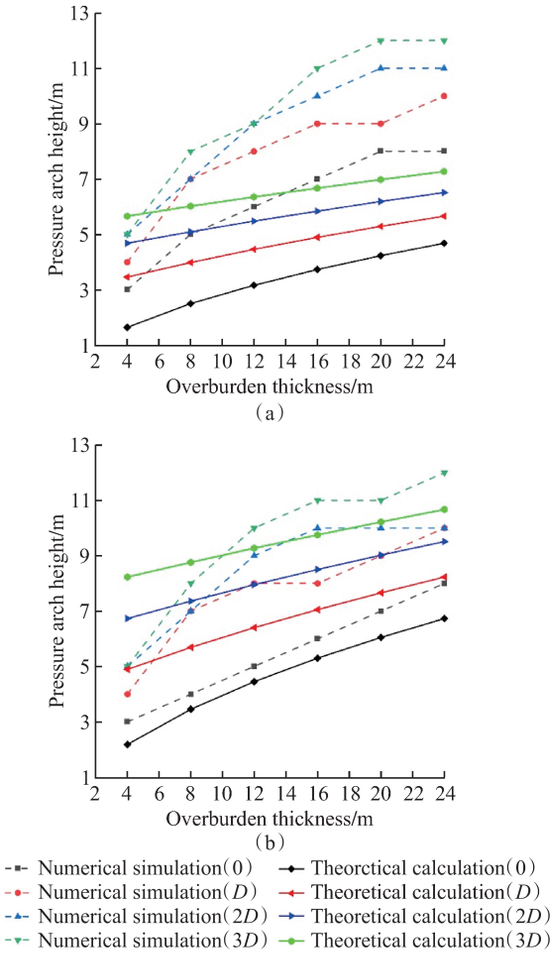

Fig. 14 Comparison of overburden thickness across various surrounding rock classes. (a) Class Ⅱ; (b) Class Ⅲ

Table 5 Comparison of minimum overburden thickness in some sections of the Xibao Interval m

Cross section No.	C1	C2	C3	C4	C5	C6	C7	C8
Simulation results	5.48	5.48	9.14	7.31	5.48	7.31	9.14	7.31
Theoretical results	5.57	6.70	8.83	7.94	5.45	6.52	8.74	8.84

As shown in Figs. 14 and 15 for identical surrounding rock classes and soft soil thicknesses, an increase in the overburden thickness moves the bifurcation point of vertical and soil self-weight stresses (along Path *a*) further from the ground surface. This indicates that higher overburden thickness mitigates the tunnel excavation effect on the vertical stress above the vault, while the maximum vertical stress increases with the expanding overburden thickness .

For Classes Ⅱ and Ⅲ rock surroundings, the thickness of soft soil of *D* resulted in a distance (0.286-0.389 times the burial depth) between the pressure arch outer boundary and its apex. An increase in the thickness of soft soil to 2*D* reduced this distance to 0.208-0.281 times the burial depth. Further, the thickness of soft soil

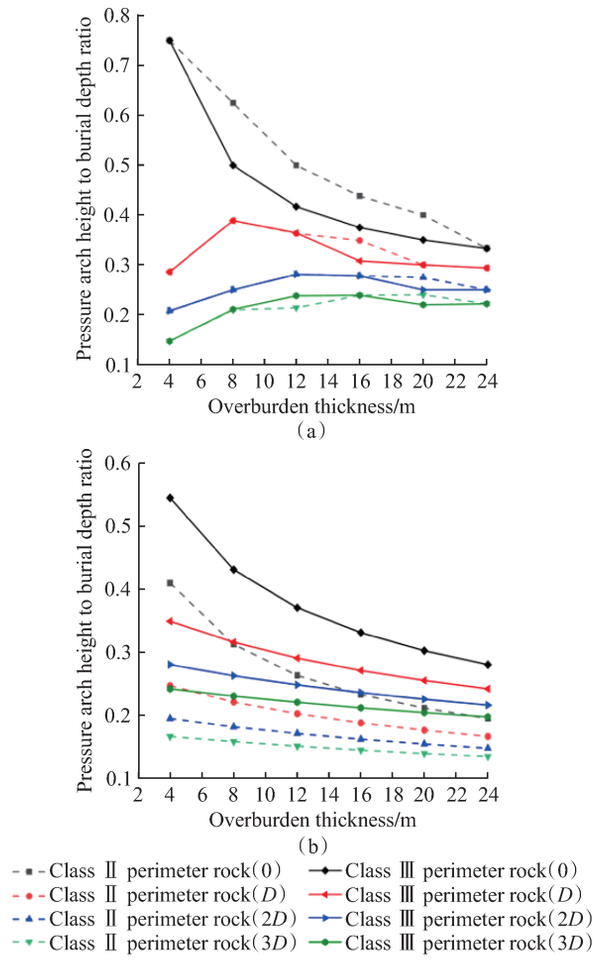

Fig. 15 Relation curves between pressure arch height and buried depth ratio of different methods. (a) Simulation results; (b) Theoretical results

of 3*D* maintained the distance at 0. 147-0. 239 times the burial depth. This trend indicates that the distance first increases before decreasing as the thickness of soft soil increases. Notably, the ratio of the pressure arch outer boundary to its burial depth decreases as the thickness of soft soil increases, with the maximum ratio corresponding to a greater thickness of the overlying rock.

Regardless of the variations in the thickness of soft soil, the ratio of the height of the pressure arch to the burial depth obtained via theoretical formulations and numerical simulations converges after the overburden thickness reaches 1. 2*D*. Before this threshold, both methods only align when the thickness of soft soil is 0 m. Although the results of the numerical simulation do not exactly match the theoretical formulation, they maintain significant consistency. As *D* of the numerical simulation is 10 m, the relationship between the pressure arch height and the radius is shown in Figs. 14 and 15, illustrating that the trends of the theoretically and numerically derived ratios are consistent and validating the theoretical formula.

At the overburden thickness of less than 1. 2*D*, the influence of the thickness of soft soil on the pressure arch height increases significantly because the low elastic modulus of the soft layer reduces the stress transfer efficiency, requiring a greater the pressure arch height to compensate for stability. When the overburden thickness exceeds 1. 2*D*, the interaction effect weakens significantly, the self-weight of the overburden dominates the stress field, the stress-absorbing effect of the soft layer is overshadowed, and the pressure arch tends to develop stably. High-class surrounding rocks exhibit reduced soft layer sensitivity: the pressure arch height only increases slightly as the overburden thickness increases. Conversely, low-class surrounding rocks exhibit significantly increased soft layer sensitivity: for the same overburden thickness variation, the pressure arch height increases significantly because low-class surrounding rocks exhibit weak inherent bearing capacity. Additionally, the stress disturbance from the soft layer further amplifies the demand for pressure arch development, thereby enhancing the interaction effect.

This difference mainly stems from the fact that the numerical model addresses local heterogeneity, nonlinear deformation, and near-joint stress concentration, resulting in slightly higher computed stress values in certain zones. Conversely, the theoretical formula adopts simplifying assumptions: it idealizes the surrounding rock as an equivalent continuous elastic arch and applies plane strain conditions, which neglect joint-induced local discontinuities and 3D stress redistribution. The relative deviation between the theoretical predictions and numerical results is generally within a reasonable range, indicating acceptable agreement between the two approaches and verifying the rationality of the proposed theoretical formula framework.

Next, eight cross-sections in the Xibao Interval are verified using the pressure arch numerical simulation method. Fig. 16 shows a comparative graph of the reasonable overburden thickness obtained via the pressure arch method, the theoretical formula method, and measured values. Notably, no evident regulations are observed in the domestic codes regarding the overburden thickness for TBM hard-rock tunneling. Relevant design institutions, relying on engineering experience, typically recommend an overburden thickness range (the minimum vertical distance between the tunnel crown and the ground or seabed surface) of 3-5 m. Notably, the measured overburden thickness in this study includes the grouting thickness of the strongly weathered grooves, which actually exceeds the proposed empirical range. However, the theoretically obtained values are generally greater than but close to the measured ones. Therefore, the results from the theoretical formula in this study are directly applicable to practical engineering, providing a reliable calculated value for the minimum overburden thickness.

Despite exhibiting significant applicability, the pro-

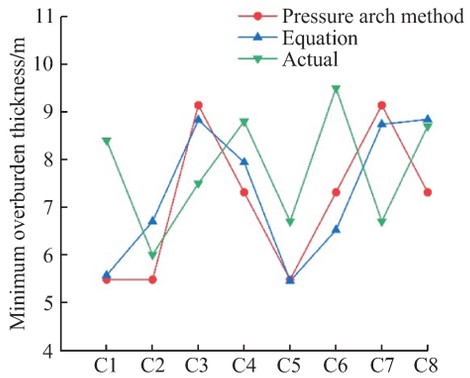

Fig. 16 Comparison diagram of reasonable overburden thickness

posed theoretical formula for pressure arch thickness also exhibits limitations. It represents an attempt to calculate the minimum overburden thickness for TBM tunneling, providing a foundation for the subsequent optimization of the calculation formula for the minimum overburden thickness.

3.4 Parameter sensitivity analysis

To investigate the influences of the surrounding rock classes, overburden thickness, and soft soil thickness on the minimum overburden thickness of TBM-excavated tunnels, three factors were subjected to parameter sensitivity analysis, following numerical simulation-based orthogonal experiments. The results were shown in Table 6.

The above results were processed using range analysis and variance methods, yielding the following range analysis table and variance analysis table, as shown in Tables 7 and 8.

As shown in Table 7, the three factors exhibited the following magnitude range order: $R_2 > R_3 > R_1$. That is, the sensitivity levels of the three factors to the minimum overburden thickness are in a descending order as: soft soil thickness, overburden thickness, and surrounding rock class.

For the minimum overburden thickness, smaller values are typically preferred. The optimal levels of each factor are selected based on the magnitude of k_{ij}. Thus, when the surrounding rock class is set to Class Ⅲ, the soft soil thickness is 0 m; the overburden thickness is 4 m; the minimum overburden thickness can be minimized. However, in actual construction, parameter values need to be determined based on actual site conditions to mitigate the uncertainty in the safety factor, the soft soil thickness.

The adopted confidence levels for the variance analysis of this orthogonal experiment are at significance levels ($\alpha = 0.05, 0.01$). Assuming the calculated F-value satisfies $F > F_{0.01}(n_1 - 1, n - 1)$, where n_1 and n are the level of each factor and the total number of experiments, respectively, the test result for that factor rejects the null hypothesis at $\alpha = 0.05$.

The following critical F-values were obtained from the F-distribution table for the corresponding degrees of freedom ($n_1 - 1, n - 1$): $F_{0.01}(2, 21) = 5.785$, $F_{0.05}(2, 21) = 3.465$, $F_{0.01}(3, 21) = 4.880$, $F_{0.05}(3, 21) =$

Table 6 Orthogonal array and experimental results m

No.	Rock class	Soft soil thickness	Thickness of overlying rock	Rock cover thickness
1	Ⅱ	0	0.4D	3
2	Ⅱ	D	0.8D	7
3	Ⅱ	2D	1.2D	9
4	Ⅱ	3D	1.6D	11
5	Ⅱ	0	2.0D	8
6	Ⅱ	D	2.4D	10
7	Ⅱ	2D	2.4D	11
8	Ⅱ	3D	2.4D	12
9	Ⅲ	2D	1.6D	10
10	Ⅲ	3D	1.2D	10
11	Ⅲ	0	0.8D	4
12	Ⅲ	D	0.4D	4
13	Ⅲ	2D	2.4D	10
14	Ⅲ	3D	2.4D	12
15	Ⅲ	0	2.4D	8
16	Ⅲ	D	2.0D	9
17	Ⅳ	0	2.0D	7
18	Ⅳ	D	2.4D	9
19	Ⅳ	2D	2.4D	11
20	Ⅳ	3D	2.4D	13
21	Ⅳ	2D	0.4D	7
22	Ⅳ	3D	0.8D	10
23	Ⅳ	0	1.2D	5
24	Ⅳ	D	1.6D	8
25	Ⅱ	0	2.4D	8
26	Ⅲ	D	2.4D	10
27	Ⅳ	2D	2.4D	11
28	Ⅳ	3D	2.0D	13
29	Ⅳ	0	1.6D	6
30	Ⅳ	D	1.2D	7
31	Ⅳ	2D	0.8D	8
32	Ⅳ	3D	0.4D	9

Table 7 Range analysis results

Statistic	Level No.	Surrounding rock class	Soft soil thickness	Overlying rock thickness
K_{ij}	1	79	49	23
	2	77	64	29
	3	124	77	31
	4		90	35
	5			37
	6			125
k_{ij}	1	8.8	12.3	5.8
	2	8.6	16	7.3
	3	8.9	19.3	7.8
	4		22.5	8.8
	5			9.3
	6			10.4
R_i		0.3	10.2	4.6

Table 8 Variance analysis results

Factor	Quadratic sum	Degree of freedom	Mean square deviation	F-value
Surrounding rock class	0.5	2	0.25	2.273
Soft soil thickness	115.8	3	38.60	350.909**
Thickness of overlying rock	83.3	5	16.66	151.455**
Error	2.4	21	0.11	
Summation	202.0	31		

Note:** represents a factor with a strong influence and high sensitivity.

3.075, $F_{0.01}(5,21) = 4.045$, and $F_{0.05}(5,21) = 2.685$. Thus, the surrounding rock class is considered a low-sensitivity factor, whereas the soft soil thickness and overburden thickness emerge as high-sensitivity factors. Based on the F-values, the sensitivity levels of the factors are in a descending order as: soft soil thickness, overburden thickness, surrounding rock class, which is consistent with the range analysis.

4 Conclusions

This paper derives a formula for calculating the minimum overburden thickness of hard-rock TBM tunnels based on the theory of arch formation in the surrounding rock. The formula is subsequently validated using data from numerous domestic and international tunnels. A comparison is made between the results from the theoretical formula and the numerical simulation results of actual cases. The theoretical model established in this study is based on the 2D plane strain and equivalent continuum medium assumptions, and it is mainly applicable to TBM tunnels in medium-to-shallow-buried hard rock or relatively intact rock masses. Since the model does not significantly account for the effects of factors such as joint development, 3D end effects, and groundwater pressure, its results should be calibrated by combining numerical analysis and engineering experience under complex stratum conditions or in significantly heterogeneous surrounding rocks. Analysis of the determining factors associated with the formula leads to the following conclusions:

(1) In the self-supporting arch formula method, at a fixed surrounding-rock class, the radius of the tunnel correlates positively with the self-supporting arch thickness, whereas the depth of the tunnel correlates positively with the square of this thickness. Conversely, at a fixed depth of the tunnel, the surrounding rock class correlates negatively with the thickness of the self-supporting arch, whereas the radius of the tunnel maintains a positive correlation with it. The formula-calculated self-supporting arch thickness is smaller than the actual depth of the tunnel of tunnels internationally, indicating that the proposed theoretical formula is relatively conservative, as the minimum overburden thickness calculated using it is also lower than that measured in actual TBM tunnels. This difference range represents a reasonable safety margin that is consistent with standard engineering practices, ensuring that the proposed method provides safe estimation results and maintains practicality. Furthermore, the applicability of this theoretical framework is mainly limited to TBM tunnels excavated in medium-to-hard rock strata under shallow to moderate burial depth conditions. For tunnels in soft rock, fractured rock masses, or water-bearing strata, the theoretical results must be supplemented with numerical analysis or empirical calibration.

(2) In cases where the tunnel is situated in Class Ⅱ or Class Ⅲ surrounding rock, the height of the pressure arch initially increases with the overburden thickness, eventually approaching a critical value equivalent to twice the diameter of the tunnel. The numerical simulation results align with the theoretical formula regarding the trend of pressure arch height changes, thereby validating the rationale of the proposed theoretical formula.

(3) The conclusions of this study are mainly based on results obtained via theoretical derivations and numerical simulations, with parameter values primarily derived from typical engineering geological reports and previous studies. Although the calculation results are consistent with outcomes derived from relevant engineering experience, they have not been directly verified using on-site monitoring data. Therefore, future studies must focus on comprehensive parametric analysis, incorporating 3D numerical simulations, the discrete element method, and the optimization of engineering experience.

References

[1] DENG M J, TAN Z S. Study on surrounding rock classification and supporting systems of TBM tunnels[J]. Tunnel Construction, 2024, 44(2): 205-224. (in Chinese)

[2] ZHANG P, REN S, WU F, et al. Prediction method of rockburst in deep buried tunnel based on multi-source data fusion[J]. Journal of Southeast University(Natural Science Edition), 2024, 54(3): 707-716. (in Chinese)

[3] CHEN D Y, LI L P, WANG J, et al. Research on back-fill grouting quality detection of shield tunnel based on impact-echo method[J]. Journal of Southeast University(Natural Science Edition), 2025, 55(1): 213-221. (in Chinese)

[4] LIN J C, SUN W Y, LI G Y, et al. Seismic fragility of shallowly buried bias loess tunnels based on vector-valued intensity measures[J]. Journal of Southeast University(Natural Science Edition), 2024, 54(2): 432-440. (in Chinese)

[5] DENG M J. Key techniques for group construction of deep-buried and super-long water transfer tunnel by TBM [J]. Chinese Journal of Geotechnical Engineering, 2016, 38(4): 577-587. (in Chinese)

[6] NILSEN B. Empirical analysis of minimum rock cover for subsea rock tunnels [J]. Developments in Geotechnical Engineering, 1993, 74: 677-687.
[7] HWANG J H, LU C C. A semi-analytical method for analyzing the tunnel water inflow [J]. Tunnelling and Underground Space Technology, 2007, 22(1): 39-46.
[8] State Administration of Coal Industry. Code for coal pillar setting and coal extraction under pressure for buildings, water bodies, railways and main shafts/tunnels [S]. Beijing: China Coal Industry Publishing House, 2017. (in Chinese)
[9] SUN W X, LIU H L, ZHANG W G, et al. Investigation on overburden thickness considering face and anti-floating stability of shallow shield tunnel [J]. Computers and Geotechnics, 2023, 160: 105562.
[10] LI S C, LI S C, ZHANG J, et al. Study on numerical method for the minimum rock covers of subsea tunnels [J]. Chinese Journal of Geotechnical Engineering, 2006, 28(10): 1304-1308. (in Chinese)
[11] SUN X H, MIAO L C, LIN H S. Numerical simulation research on excavation face stability of different depths of shield tunnel [J]. Journal of Southeast University (Natural Science Edition), 2017, 47(1): 164-169. (in Chinese)
[12] PANG L F, LIU W T, QIN Y Y. Analysis of main controlling factors of overburden failure in coal mining under thick coal seam geological conditions [J]. Geotechnical and Geological Engineering, 2021, 39(2): 883-896.
[13] DONG Y, HUANG Y C, DU J F, et al. Study on overburden stability and development height of water flowing fractured zone in roadway mining with cemented backfill [J]. Shock and Vibration, 2021, 2021(1): 6661168.
[14] LIU S G, LI K X, SHI W P, et al. Analysis of mining subsidence characteristics and deformation prediction considering size parameters and mechanical parameters [J]. Geofluids, 2022, 2022(1): 5495509.
[15] PENG Z Z, FENG K, XIAO M Q, et al. Reasonable overlying thickness of subaqueous tunnels based on pressure arch theory [J]. Rock and Soil Mechanics, 2018, 39(7): 2609-2616. (in Chinese)
[16] WANG F, CHEN T, CHEN Z T, et al. Failure analysis of overlying strata in fault fracture zone during coal mining [J]. Journal of Geophysics and Engineering, 2023, 20(6): 1127-1139.
[17] MA C, GUO X Q, ZHANG L Y, et al. Theoretical analysis on stress and deformation of overburden key stratum in solid filling coal mining based on the multilayer winkler foundation beam model [J]. Geofluids, 2021, 2021(1): 6693888.
[18] YANG Y K, MA Y R, JI C X, et al. Effect of mining thickness on overburden movement and underground pressure characteristics for extrathick coal seam by sublevel caving with high bottom cutting height [J]. Advances in Civil Engineering, 2018, 2018(1): 6871820.
[19] PAN H S, DU G Y, WANG K, et al. Model test and numerical simulation on pressure arch of unlined loess tunnel 1 [J]. Journal of Southeast University (Natural Science Edition), 2019, 49(5): 949-955. (in Chinese)
[20] CHEN N. Research on determination method of overburden thickness of Rongjiang Forth Road Underwater Tunnel [D]. Nanchang: Jiangxi University of Science and Technology, 2021. (in Chinese)
[21] WU M F, ZHANG H J, QIU W G. Study on how to distinguish between deep and shallow tunnels with large profile [J]. Modern Tunnelling Technology 2010, 47(4): 1-5, 26. (in Chinese)
[22] LÜ Y, LIANG G S, LU L N, et al. An analytical study of the range of pressure arch arches in circular tunnels with surrounding rock [J]. West-China Exploration Engineering, 2016, 28(10): 165-169. (in Chinese)
[23] ZHOU X J, WANG J H, LIN B T. Study on calculation of rock pressure for ultra-shallow tunnel in poor surrounding rock and its tunneling procedure [J]. Journal of Modern Transportation, 2014, 22(1): 1-11.

基于围岩成拱理论的TBM掘进最小覆岩厚度理论模型与数值模拟研究

周中，隋玉超，鄢海涛

（中南大学土木工程学院，长沙 410075）

摘要：基于围岩成拱理论与无铰拱结构理论，推导得到最小覆岩厚度理论公式，并将国内外多条隧道的不同力学特征代入该公式，得到不同围岩等级下的最小自承拱公式。依托实际双模盾构隧道工程案例，建立TBM模式开挖的数值模型，用以验证理论公式。设置3个围岩等级、4个土层厚度梯度和12个覆岩厚度梯度，通过三因素组合形成144个模型，开展均匀试验，得到不同围岩等级下的压力拱高度。结果表明，理论公式中隧道半径与压力拱高度成线性正相关关系，隧道埋深与压力拱高度的平方成线性正相关关系。数值模拟中压力拱高度随覆岩厚度增加而增大，最终趋于一个2倍洞径的临界值。数值结果与理论公式结果吻合良好，从而验证了理论公式的合理性。

关键词：最小覆岩厚度；TBM；压力拱；数值模拟；自承拱

中图分类号：U45